Quasi-degenerate states and their dynamics in oxygen deficient reducible metal oxides

Nathan Daelman, Franziska Simone Hegner, Marcos Rellán-Piñeiro, Marçal Capdevila-Cortada, Rodrigo García-Muelas, and Núria López[a)]

AFFILIATIONS

Institute of Chemical Research of Catalonia, ICIQ, The Barcelona Institute of Science and Technology, BIST, Av. Països Catalans 16, 43007 Tarragona, Spain

[a)]**Author to whom correspondence should be addressed:** nlopez@iciq.es

ABSTRACT

The physical and chemical properties of oxides are defined by the presence of oxygen vacancies. Experimentally, non-defective structures are almost impossible to achieve due to synthetic constraints. Therefore, it is crucial to account for vacancies when evaluating the characteristics of these materials. The electronic structure of oxygen-depleted oxides deeply differs from that of the native forms, in particular, of reducible metal oxides, where excess electrons can localize in various distinct positions. In this perspective, we present recent developments from our group describing the complexity of these defective materials that highlight the need for an accurate description of (i) intrinsic vacancies in polar terminations, (ii) multiple geometries and complex electronic structures with several states attainable at typical working conditions, and (iii) the associated dynamics for both vacancy diffusion and the coexistence of more than one electronic structure. All these aspects widen our current understanding of defects in oxides and need to be adequately introduced in emerging high-throughput screening methodologies.

I. INTRODUCTION

Transition and rare-earth metal oxides have attracted much attention because of their versatile chemical and physical properties, spanning the whole range from conductors to semiconductors and wide gap insulators.[1,2] This results in a large manifold of exciting catalytic, electrocatalytic, and even photo-catalytic activity in important reactions, as first illustrated in the water oxidation by Fujishima and Honda.[3] Oxygen defects are crucial in defining these properties, which has been highlighted in many reports.[4–7] While entropic reasons dictate that all solid crystals must contain a certain proportion of defects at non-zero temperature,[2,8] this is particularly acute for oxides because they are typically synthesized via heating at high temperatures.[1,9,10] This procedure generates oxygen depletion, which provokes severe changes in the material properties and can be monitored, for instance, in the reduction of the work function.[11]

Consequently, the understanding of the electronic structure of defective oxides is key, not only to optimizing and fine-tuning their performance but also aiding the design of novel materials with tailored properties.[2,4] Yet, many computational approaches are based on describing pristine (non-defective) structures and, thus, most of the rich chemical complexity is simplified below the levels of proper predictions.[12,13] Importantly, most of these simulations on non-defective materials lie at the core of search engines of large databases and machine learning algorithms.[14–20] In order to properly account for chemical and physical attributes, better theoretical tools to assess structural defects have to be developed and implemented in those high-throughput approaches.[21–24] In the present perspective, taking some established examples from the literature, we aim at defining new rules to include defects in such studies.

Oxides can be analyzed following the standard classification in terms of reducibility,[25] as depicted in Fig. 1. Here, the bandgap acts as a general descriptor for the metal–oxygen bond and reducibility. Highly ionic, non-reducible binary oxides, as those derived from alkaline earth metals or aluminum, present simple electronic structures with wide bandgaps and are, thus, effective insulators. The fully

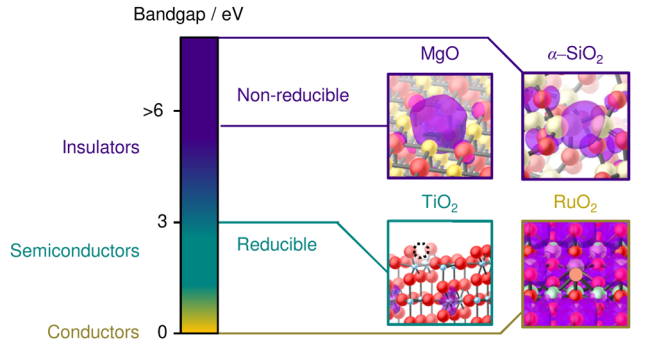

FIG. 1. Traditional classification of metal oxides described by their bandgap. In the covalent oxide α-quartz (SiO_2) with a very large bandgap, excess electrons may localize in a newly formed Si–Si bond upon reconstruction. Non-reducible, oxides such as MgO have large bandgaps and behave as insulators. Upon oxygen removal, they form color centers where excess electrons are trapped at vacancy sites. By contrast, reducible oxides typically have narrow bandgaps and behave as semiconductors. Their vacancy formation energies are smaller as excess electrons tend to partially localize at metal centers and reduce them. In the example, excess electrons on TiO_2 reduce two non-neighboring Ti atoms in the sub-surface. In the limit of zero bandgap, a conductive oxide, such as RuO_2,[49] delocalizes excess electrons around the surface.

ionic model adequately predicts their properties, such as vacancy formation energies and diffusion barriers, which tend to be high in energy for those materials.[26,27] For these oxides, once the oxygen atoms are removed from the lattice, the two excess electrons are stored in the cavity left by the O atom.[4] Such bound electrons are found, for instance, in defective MgO and give rise to additional optical absorption lines, from which their name *color centers* or *F* centers (from German *Farbe* = color) was derived.[2,8]

In covalent oxides, such as SiO_2, the additional electrons left upon oxygen removal remain as dangling bonds of sp^3 character at the Si center or the defect is quenched by forming homoatomic bonds, e.g., Si–Si units, as shown in Fig. 1.[28–31]

In reducible oxides, the electronic structure is more intricate and oxygen vacancies tend to be electronically active.[5,25] Due to the significant amount of covalency, cationic and anionic contributions cannot be easily disentangled, and a clear one-to-one mapping of formal charges and computed ones is not possible.[32] Many reducible oxides behave as semiconductors, i.e., the valence and conduction bands are separated by a small energy gap (below 4 eV). In these materials, the vacancy formation energies are smaller than in non-reducible metal oxides as the electrons left by oxygen removal end up reducing the metal centers and populating otherwise forbidden electronic states. This change in electron occupation typically causes a mismatch in the ionic radii and induces a local lattice deformation, also known as a polaron.[33,34] Depending on the strength of the electron–phonon coupling and the energy difference between the vacancy-induced electronic states and the conduction band, electron transport may occur via polaron hopping or band-like conduction.[13,35] The oxygen vacancy can therefore act as an effective *n*-type dopant, which is beneficial for many (photo-)electrochemical applications.[6] Not only electronic but also ionic conduction may take place via oxygen vacancy migration.[36]

One of the best known reducible metal oxides is TiO_2 in its three polymorphs, rutile, anatase, and brookite.[3,37,38] Upon oxygen removal, two Ti centers are reduced to Ti^{3+}, which have electronic states close to the conduction band,[39–41] forming mobile polarons, as was observed during *ab initio* molecular dynamics simulations.[42] The extent of the formed polarons and the interplay between trapping and detrapping of the excess charge is largely dependent on the exposed surface facet.[39,41,43] Furthermore, TiO_2 and many other reducible oxides can easily lose more than one oxygen and store the deficiencies along one particular direction (glide planes), known as Magnéli phases.[2,44] The clustering of oxygen vacancies leads to broad distributions of electronic states in the bandgap and has a crucial impact on the applications as catalysts,[45] photoelectrodes, or charge transport layers.[46–48]

However, the situations described above are far too simple for the characterization of vacancies in many other defective metal oxides. Removing oxygen may lead to different geometric as well as electronic configurations with similar energies, i.e., quasi-degenerate states. In other words, one single vacancy state is not enough to account for the complexity of many oxides at finite temperatures, where a dynamic equilibrium between multiple configurations is present. In this perspective, we showcase four relevant metal oxides, namely, CeO_2,[50–52] In_2O_3,[53,54] MoO_3,[55] and $BiVO_4$,[56,57] which exhibit quasi-degeneracy. The understanding of their complex electronic structures is essential not only to improve their catalytic efficiencies but also to expand that knowledge to other reducible metal oxides. With this perspective, we aim at giving a guideline to improve current high-throughput approaches, which shall screen for possibly advantageous defective oxides and include the possibility of quasi-degenerate structures.

II. THEORETICAL APPROACHES

Density functional theory (DFT) is the workhorse of electronic structure simulations due to its favorable scaling and high (close to chemical) accuracy, providing practical estimates for the ground state energy and electron density of many-electron systems.[58–60] Its implementations differ in the description of the so-called exchange–correlation functional that is analytically unknown. Most commonly applied for metal oxides are functionals based on the Generalized Gradient Approximation (GGA), including PW91,[61] PBE,[62] and their revised versions revPBE,[63] RPBE,[64] and PBEsol.[65] The latter two typically yield more accurate adsorption energies or lattice parameters, respectively.[66] However, GGA often fails in accurately describing the electronic properties of reducible oxides due to its inherent self-interaction error,[67] in which one electron interacts with itself in an unphysical manner. This leads (i) to overdelocalization of the electronic density, overestimating the degree of covalency in the system, and (ii) to a systematic underestimation of the bandgap. The latter is particularly severe for small bandgap semiconductors since they are often incorrectly predicted to be metals. The error becomes relevant for elements with strongly correlated electrons, such as transition metals and rare-earth elements with d- and f-electrons.

The most common and computationally cheapest approach to mitigating the self-interaction error is to add an energy penalty to the functional that accounts for the on-site interaction between localized electrons.[8,68,69] This is the so-called Hubbard *U* correction.[70] It

is selectively applied to certain atomic sites in the lattice, typically to the metal cations with strongly localized electrons but sometimes also for contributions coming from anions.[71–73] In the most popular implementation of DFT+U, Dudarev's approach, the Coulomb and exchange interaction terms are reduced to a single parameter, the effective Hubbard term U_{eff} = U.[74] It can be formulated as

$$E_{\mathrm{DFT}+U} = E_{\mathrm{DFT}} + U_{eff}\frac{1}{2}\sum_{l}(\rho_l - \rho_l^2). \quad (1)$$

Here, the sum runs over the occupation values (ρ_l) of the atomic orbitals with the angular quantum number l. DFT+U is able to accurately describe reducible transition and rare-earth metal oxides; yet, the choice of U is not trivial and largely depends on the system and atomic occupancies and, therefore, on the charge associated with the cations.[75,76] Its value can be derived in a standalone fashion using a linear response approach to balance out the derivative of the atomic chemical potentials.[75,77] In many practical cases though, U is instead fitted to the bandgap[78] or redox energies[79] from experiments or higher levels of theory (e.g., hybrid functionals), either alone or coupled to the thermodynamics of some processes.[76,80,81]

One of the drawbacks in assessing oxygen vacancy formation using the Hubbard correction is the U dependence on the local electronic environment.[76] In principle, the U parameters for the metal sites surrounding the vacancy should differ from those that are unaffected by it. Hybrid functionals circumvent this issue, introducing non-locality in the exchange-correlation energy by incorporating a certain amount of exact exchange E_X^{HF} from Hartree–Fock theory.[82] Compared to DFT+U, this is a rather computationally expensive procedure (1–2 orders of magnitude larger); however, the implementation of these approaches in periodic codes has improved over the last years and are nowadays becoming routine (except for dynamic properties). Out of those, commonly used for solids are the full-range PBE0[82] and range-separated HSE (HSE03/HSE06)[83] functionals, the latter replacing long-range exchange by DFT exchange, which allows for smoother convergence. Like most hybrid functionals, they employ a fraction of 25% E_X^{HF}.[82,83] This has shown to be too much for several transition metal containing oxides as it leads to overestimated band splittings, including exceedingly large bandgaps, and to a nonphysical stabilization of high spin states.[20,84–87] Defect levels[88,89] and polaron hopping barriers,[86] and therefore, the localization of excess charge, are crucially dependent on the amount of E_X^{HF} introduced. The optimum fraction $a(E_X^{HF})$ of exact exchange can be obtained through empirical fitting to experimentally measured constants, such as bandgaps[85] or polaron hopping barriers,[86] but it can also be calculated self-consistently[90,91] or approximated by $a(E_X^{HF}) \approx \frac{1}{\epsilon_\infty}$ for many oxide semiconductors.[88,89] Typically, 10%–15% of E_X^{HF} was found to describe well the electronic structures of transition metal oxides,[85–87,92] as well as rare-earth metal oxides.[91,93]

To achieve a more accurate description of defect states in reducible oxide semiconductors, it is necessary to go beyond density functional theory. By definition, the electronic structure of excited states, i.e., the conduction band properties, cannot be assessed by ground state DFT. Many-body perturbation theory, such as the GW method, can determine the quasiparticle band structures and excited state properties with high precision,[94,95] but its implementation is yet limited due to its large computational cost and required proficiency. Instead of fully self-consistent GW, typically non-self-consistent G_0W_0 calculations are applied on top of DFT or hybrid functional results. Those may, however, not necessarily improve the accuracy of defect levels, when compared to hybrid functional calculations.[96]

III. INTRINSICALLY DEFECTIVE STRUCTURES

Bulk CeO_2 presents a simple fluorite structure, as shown in Fig. 2(a). Its experimental bandgap is 3.2 eV,[97,98] and vacancy formation was computed to require 1.85 eV with respect to gas-phase molecular oxygen.[52] Upon oxygen removal, two separate

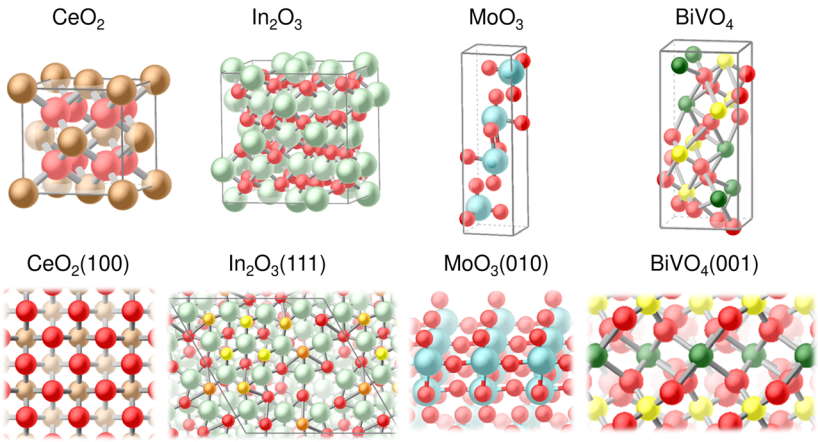

FIG. 2. Overview of the case studies presented here: CeO_2, a charge carrier, and its (100) polar surface prior to reconstruction; the highly anisotropic In_2O_3, commonly used doped with Sn (ITO) in optoelectronic devices and recently characterized as a selective catalyst for CO_2 reduction; MoO_3, commonly used as a catalyst in the Formox process and hydrodeoxygenation reactions; and $BiVO_4$, a light-harvesting catalyst with high potential for photo-electrochemical water oxidation. The color scale of In_2O_3(111) emphasizes the anisotropy and refers to the abstraction energy of a surface oxygen atom to form water in H_2-rich atmospheres.[115]

Ce atoms are reduced, populating the 4f subshell in between the valence and the conduction band. Consequently, their ionic radii increase. The material can be employed either as a support, for instance, in a three-way car-exhaust catalyst,[99] or as a catalyst itself, for example, in high temperature HCl oxidation to chlorine[100] and other chlorinated structures,[101] or the production of carbamates.[102]

Many of the appealing catalytic properties of ceria stem from its facile reducibility and innate oxygen transport ability at the surface. Similar to TiO_2,[39,41,103] the surface orientation determines the most likely position of the oxygen vacancy on ceria. In the case of CeO_2(111), the most exposed surface on polycristalline[52] and rod-shaped[104] nanoparticles, its oxygen vacancies migrate to the subsurface positions, while the electrons reside at the surface cerium centers to avoid nearest neighbor interactions.[105–108] There they affect intrinsic properties including the basicity of the surface and the redox potential, as well as mesoscopic parameters, such as its wettability.[109] Some of these properties can be fine-tuned via doping.[52]

Nanocubes, by contrast, preferentially exhibit the polar (100) termination, shown in Fig. 2. Cuts along these directions generate a type 3 surface[110] according to the Tasker polarity rules.[111] They require a substantial reconstruction to become stable so that the top surface layer expels half of its oxygen atoms. Since this process strives toward overall surface neutrality and a minimal dipole moment, no cation reduction occurs as a result. As such, the surface does not present any defect state in the bandgap, which can be seen in Fig. 4. The oxygen depletion of the purely O-terminated surface was originally considered to yield a regular pattern, where rows of top-surface oxygen atoms run parallel and are interspersed with the vacancies that act like trenches.

The high oxygen vacancy mobility in bulk ceria extends to the (100) surface vacancies. The low coordination number along with newly liberated space allows for an increase in the thermal fluctuations of the low-lying soft modes of the oxygen atoms. With the number of particles (O atoms) reduced to half the number of boxes (potential O-positions) and low kinetic barriers, other potential O-configurations become accessible on the reconstructed (100) surface. *Ab initio* molecular dynamics support this claim, demonstrating that the diffusion starts at temperatures below 500 K, as shown in Ref. 112.

The configuration phase space of these patterns does not have one single low-energy outlier. Rather, all the structures appear with a very small energy spacing, resulting in a densely packed configuration space. For instance, the second lowest configuration in energy presents a zigzag O-pattern and has a surface energy of only 0.01 J/m^2 higher than the row pattern. Because its multiplicity (the number of identical zigzag structures) is larger than one, it contains a new, configurational entropy term. The surface, thus, has many degrees of freedom in terms of oxygen configurations, and the contribution from their entropies renders the oxygen-termination more stable.[112] *In situ* HRTEM experiments confirmed the presence of variable terminations.[113]

Finally, the coexistence of different local geometries also provides a wider array of anchor points for complex reactants to adsorb onto the surface, radically changing the reactivity of this surface. This is the case when stabilizing single metal adatoms.[114] The geometric isolation from the other metals on the surface, together with the strong coupling to the electronic structure of the oxide material, provides a new mechanism for the metal/support interactions.

IV. VACANCIES IN ANISOTROPIC ENVIRONMENTS

In_2O_3 is an example of intrinsic structural complexity, which is mainly used in optoelectronic devices in combination with Sn (ITO) to improve its electrical conductivity.[53,116,117] It can be a transparent, conductive oxide meaning that it has a high electrical conductivity and that it is nearly transparent in the visible region.[53] In_2O_3 is also a selective catalyst for reactions such as propane dehydrogenation to propene,[118] acetylene semi-hydrogenation to ethylene,[115] and, most importantly, CO_2 hydrogenation to methanol.[54,119,120] It is a more cost-efficient catalyst than the noble metals as the commodity price of indium is 324 USD/kg.[121]

The bulk solid can appear in cubic (bixbyite),[122] rhombohedral (corundum),[123] and amorphous[124] forms. The bixbyite, shown in Fig. 2, is formed by a Jahn–Teller deformation of the more regular corundum structure. Yet, it can also be understood as a reconstruction of the much simpler face-centered cubic fluorite structure (CaF_2) by removing one-quarter of the oxygen atoms in a $(2 \times 2 \times 2)$ supercell.[117] The In atoms in this distorted structure appear in five non-equivalent crystallographic sites, each one surrounded by six oxygen atoms.[125]

Its most stable surface, (111),[117,126] was studied using the pure PBE functional, after having verified that the U_{eff} contribution is negligible.[115] It is highly anisotropic and can easily lose its oxygen atoms.[127,128] A close look to the surface reveals that it contains four chemically non-equivalent oxygen sites, as shown in Fig. 2.[115] In H_2-rich atmospheres, these oxygen atoms can desorb as water, with energies ranging from exothermic (−0.8 eV) to mildly endothermic (+0.4 eV). This reaction is fully reversible as the vacancies heal in the presence of water even at trace concentrations.[119,129]

Amidst the anisotropy, the three topmost positions are energetically equivalent. Vacancy diffusion to the neighboring sites shown in Fig. 2 is, therefore, thermoneutral.[128] All of these vacancies remain confined to the surface[130] because their formation in the bulk is highly endothermic. Upon formation, the surface is able to accumulate the residual electrons.[127] They partially localize onto the low-lying s- and p-states of the three exposed In atoms surrounding the vacancy,[115,119] although most of it remains delocalized,[130] as illustrated in Fig. 4. It has been shown that variations of the synthesis protocol can lead to surface hydroxide formation.[131,132] Doping strategies can modify the number of vacancies accumulated on this surface. For instance, the incorporation of Pd atoms via coprecipitation into the lattice stabilizes the formation of a cluster of vacancies.[133]

V. COEXISTING OXIDATION STATES OF THE CATION

α-MoO_3, which is shown in Fig. 2, is used for several chemical and physical applications[55] as a catalyst and photosensor. Oxygen vacancy formation in this compound is essential for maintaining the catalytic activity of the oxide in important chemical transformations, such as the Formox process (selective methanol oxidation to formaldehyde)[134–137] or hydrodeoxygenation (HDO) reactions.[138–141] These defects are in fact unavoidable, even at high oxygen pressures.[142] The formation of vacancies also influences its

physical applications since its optical properties are correlated with the vacancy concentration.[143]

The alpha phase of molybdenum trioxide is a semiconductor (3.0–3.2 eV for the experimental bandgap[144–146]), and it is formed by bilayers of distorted octahedra (along the xz plane) packed through van der Waals interactions (along the y axis). This is the cleave plane that leads to the lowest energy surface α-MoO_3(010). The structure contains three symmetrically nonequivalent O atoms in its lattice of which the terminal one is the easiest to lose.[81,147]

A PBE+U study (with U_{eff} = 3.5 eV optimized against the hybrid HSE06 functional) found that the vacancy can yield two different electronic structures. The ground state configuration of $\mathcal{V}_{Ot}$ (2.61 eV for the formation of 1/2 O_2 at a coverage of $\theta_{\mathcal{V}_{Ot}}$ = 1/9 ML) corresponds to the reduction of two Mo^{6+} centers to Mo^{5+} (2 × Mo^{5+}), the undercoordinated Mo (Mo_{cus}) and a neighboring Mo center along the [001] direction. The DOS analysis shows that each Mo center has one electron located in a d-orbital, being lower in energy than the conduction band, as shown in Fig. 4. In the second configuration (2.84 eV for the formation of 1/2 O_2 at $\theta_{\mathcal{V}_{Ot}}$ = 1/9 ML), Mo_{cus} is doubly reduced to form a Mo^{4+} center. The DOS shows that the electron pair is divided over two different d orbitals of Mo_{cus} and have the same spin (Fig. 4). The two electronic states were fully characterized showing clear differences in bond distances, Bader charges, XPS displacement, and vibrational frequencies, each usable as fingerprints. Both states and their vacancy formation energies were confirmed by hybrid HSE06 functional, which we used as a benchmark.

The ground state, thus, corresponds to a bipolaron with the two electrons localized at two Mo centers. The metastable state, on the other hand, is defined as a single dipolaron, where both electrons are stored at the same center. The coexistence of these states can be rationalized by the combination of redox and electrostatic properties of the oxide. By the addition of one and two hydrogen atoms to the surface, we found that for Mo^{5+}, the energy to oxidize it (to Mo^{6+}) and to reduce it (to Mo^{4+}) is equal but with opposite sign. Therefore, the redox process to the conversion between the 2 × Mo^{5+} and Mo^{4+} states is thermoneutral. This is also confirmed by the DOS analysis in Fig. 4 since the vacancy-induced gap electronic states have the same energy. Only the electrostatic interactions between both cations and the surrounding oxygen atoms are responsible for the different stability of both states.[81]

The predicted electronic states are in agreement with the experimental characterization of α-MoO_{3-x} surfaces,[11,148,149] where three different reduced Mo centers (six-coordinated Mo^{5+}, five-coordinated Mo^{5+}, and five coordinated Mo^{4+}) were observed. At low reduction levels, Mo^{5+} centers predominantly exist, whereas only at high reduction levels, also Mo^{4+} centers were observed.[11,138,149] We have studied the variation of vacancy formation energies with $\mathcal{V}_{Ot}$ coverage for both electronic states. The energy needed to form 2 × Mo^{5+} increases linearly with coverage, whereas it remains constant to form Mo^{4+}, until a coverage of 1/2 ML, where both energies converge. For $\theta_{\mathcal{V}_{Ot}}$ = 1/9, the Maxwell–Boltzmann distribution (at 300 °C) predicts 22.0% of Mo^{5+} centers and only 0.1% of Mo^{4+} centers on the catalyst surface. However, for $\theta_{\mathcal{V}_{Ot}}$ = 1/2 ML, more similar distributions of 19.2% Mo^{5+} and 15.4% Mo^{4+} centers are predicted.

Experimentally, it was found that polarons are highly mobile in α-MoO_3.[150,151] We found that both states are interconnected by electron hopping with an energy barrier of 0.3 eV, which can easily be overcome at typical reaction temperatures. The Born–Oppenheimer molecular dynamics were performed to illustrate the dynamic behavior of electronic states, as shown in Fig. 3. Simulations at 573 K and $\theta_{\mathcal{V}_{Ot}}$ = 1/4 ML resulted in 95% and 5% population of 2 × Mo^{5+} and Mo^{4+} states, respectively.

These two states have an immediate impact when studying the chemical properties of molybdenum. The difference in adsorption energies of methanol and formaldehyde, the reactant and product

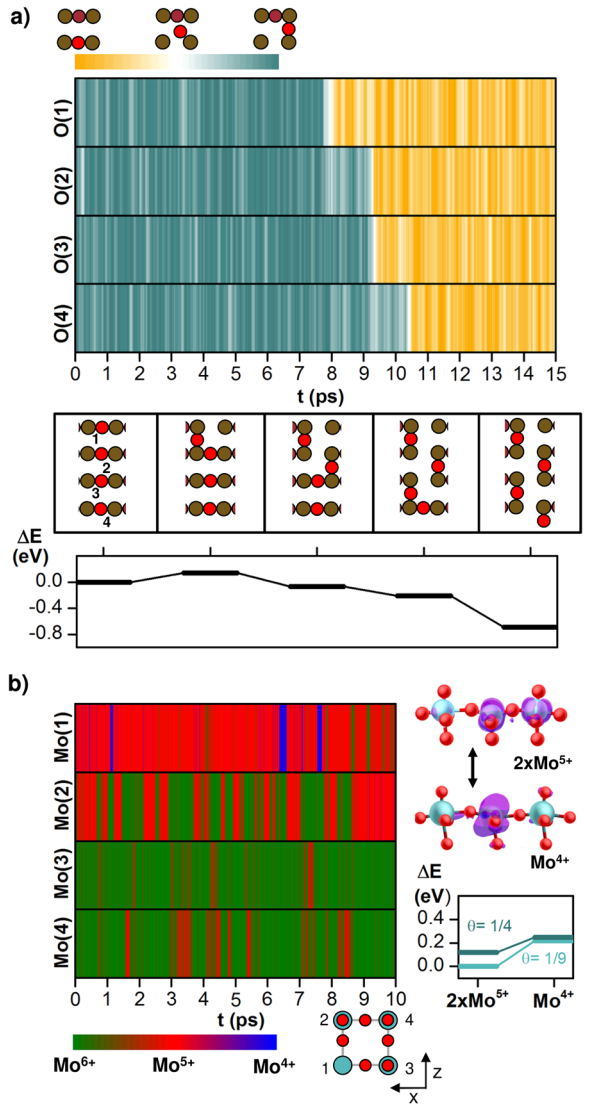

FIG. 3. (a) Position of O_s on CeO_2(100) 4 × 4 as a function of time in the Born–Oppenheimer Molecular Dynamics (BOMD) at 800 K (top). Ideal geometry of the five different structures observed during the BOMD (center). The energy profile for the structures obtained in the BOMD (bottom). (b) Local magnetization of surface Mo on molybdenum oxide as a function of time for the BOMD at 573 K and $\theta_{\mathcal{V}_{Ot}}$ = 1/4 ML (left). Structure and electron localization of the two electronic states to $\mathcal{V}_{Ot}$ and their energy profile (right). Adapted from Ref. 81.

of the industrial Formox process,[136] on a defective center of either configuration largely influences the catalytic activity. The adsorption of methanol through its lone pair on the undercoordinated center is independent of the oxidation state. However, formaldehyde also interacts with a neighboring oxygen atom, which results in an adsorption energy of 0.23 eV higher on Mo^{4+} centers. Therefore, to analyze and understand the chemistry of these materials, at least those two states are needed to present a comprehensive analysis of the reaction pathways.

VI. MULTIPLE GEOMETRIC AND ELECTRONIC CONFIGURATIONS IN A TERNARY OXIDE

A level of complexity is added in multinary oxides, for instance, in oxide perovskites, such as $SrTiO_3$,[152–154] or complex light absorbers, such as $BiVO_4$, which we discuss as a case study herein and which is shown in Fig. 2. During the last decade, $BiVO_4$ has emerged as a promising candidate for photo-electrochemical water oxidation catalyst due to its suitable bandgap and valence edge positions, as well as superior hole mobilities and charge separation efficiencies.[56,57,155,156] Nonetheless, it suffers from poor electron transport, which is ascribed to small polaron formation self-trapping the electrons.[57,86,157] Oxygen vacancies were found to increase the catalytic activity, which often is attributed to an increase in *n*-type conductivity typical for many metal oxides.[6,158–161] Being effective *n*-type dopants, they need to form electronic states at the conduction band minimum or close to it, hence becoming *shallow* donors. They can, however, also interact with the intrinsic polaronic levels and lead to enhanced polaronic transport, although they form *deep* states.[35] Oxygen vacancies may also have a detrimental effect on the photo-electrochemical behavior since they can act as charge-carrier traps and/or electron–hole recombination centers.[46,162–164] The exact role of oxygen vacancies in $BiVO_4$ is still under debate.[35,165,166] To a large extent, this is due to artifacts of the employed methods, i.e., differences in the DFT functionals, which largely impact the computed electronic structure of the vacancy.

Oxygen vacancies in the bulk and at the (001) surface have been screened with different density functionals including GGA, GGA+U, and hybrid level of theory.[92] For the hybrid study, we used the modified PBE0-10 functional that is PBE0 with only 10% of the exact exchange introduced; as for GGA(+U), we used PBEsol and, respectively, PBEsol+U with U_{eff} = 2.5 eV that has yielded good results in previous studies.[92,165,167] We assessed the electronic structure of the defective oxide, including a detailed comparison of the influence of each functional.

Importantly, we found distinct geometric arrangements of oxygen vacancies in $BiVO_4$:[92,168] localized vacancies, $\mathcal{V}_O^{\mathrm{loc}}$, with undercoordinated $V^{4+}_{cus}O_3$ and $Bi^{2+}_{cus}O_7$ units and split vacancies, $\mathcal{V}_O^{\mathrm{split}}$, in which the vacancy is quenched by forming a V_2O_7 dimer with an adjacent VO_4 unit. This is due to the flexibility of the lattice (and the ability of V to generate oligomers with oxygen), which allows for facile rotation of the VO_4 tetrahedra and, therefore, breaking and forming of V–O–V bonds between the metallic planes along the [001] direction. Such bridge formation can be viewed as VO_4 orthovanadates condensing to produce polyoxovanadates, which has been widely observed in solution,[169] as well as in solid V_2O_5, where it was found to reduce the cost of $\mathcal{V}_O$ formation.[170]

In the bulk, the different types of vacancies have similar formation energies with small functional-dependent differences, whereas $\mathcal{V}_O^{\mathrm{split}}$ is largely stabilized (≳1 eV) in the subsurface of the thermodynamically most stable (001) surface. Moreover, the transition from $\mathcal{V}_O^{\mathrm{loc}}$ to $\mathcal{V}_O^{\mathrm{split}}$ proceeds without significant barrier when O is removed from the (001) surface.[92] In the subsurface, the V–O–V formation is so favorable because (i) surface relaxation decreases the distance between the upper two metallic layers and, thus, the distance between the bridge forming V atoms and (ii) the VO_4 tetrahedra that terminate the (001) surface move and rotate more easily than fully coordinated bulk VO_4 units, regarding solely for geometrical reasons. The (001) subsurface, therefore, presents an energy sink for accumulation of oxygen vacancies in the form of V–O–V bridges, which is also supported by recent experiments detecting reduced metallic surface sites by LEED and photoemission spectroscopy.[171,172]

Formation of those different structures has tremendous consequences for the electronic properties and, therefore, for the photoelectrocatalytic activity. The resulting electronic configurations are shown in Fig. 4 on the right. In the localized vacancy, $\mathcal{V}_O^{\mathrm{loc}}$, the excess electronic charge is trapped as an electron pair at the vacancy site and at the surrounding Bi and V atoms, therefore reducing Bi^{3+} to Bi^{2+} and V^{5+} to V^{4+}. This gives a doubly occupied electronic state of around 0.9–1.2 eV below the conduction band, which is composed of a Bi 2p and V 3d hybrid orbital. Interestingly, a similar electronic configuration was obtained for all GGA, GGA+U, and hybrid functionals; however, with GGA, the trap state is less deep, lying only 0.6–0.7 eV below the conduction band.

When forming a V–O–V bridge in $\mathcal{V}_O^{\mathrm{split}}$, the surplus electrons are no longer bound as a pair but split and delocalized onto different vanadium centers. The extent of delocalization is highly dependent on the functional and local geometry. Considering the hybrid functional PBE0-10 as highest in accuracy, two isoenergetic electronic configurations were obtained, depending on the relevant V–O distances, i.e., whether the input geometry was taken from a prior PBEsol or PBEsol+U optimization. One electron always remains localized in the 3d orbitals (t_2 symmetry) of the bridge forming V with a slightly longer V–O bond, which is reduced to V^{4+}, forming a deep intragap state at ≥1.2 eV below the conduction band (with hybrid and GGA+U methods; ~0.7 eV with GGA). The second electron is either delocalized onto different V centers within the same metallic plane or the adjacent planes along the [001] direction when calculated with GGA or hybrid with GGA geometry, or localized onto the other bridging V (V^{4+}) with GGA+U or hybrid with GGA+U geometry (see Fig. 4). Other electronic configurations, where the second electron is localized on a V atom farther away from the vacancy site and, thus, forms small polarons in the bulk region of $BiVO_4$, have also been observed.[35,92] The interaction between the two additional electrons in $\mathcal{V}_O^{\mathrm{split}}$ is negligible, since both singlet and triplet states with equal energies were found. In the case where the extra electron is two-dimensionally delocalized in the metallic plane (and adjacent planes), an additional electronic state at the bottom of the conduction band (in the bulk) or very close to the conduction band ((001) surface) was found. This would favor band-like conduction via conduction band states. In the case where the second electron localizes and reduces a different V atom, a deeper

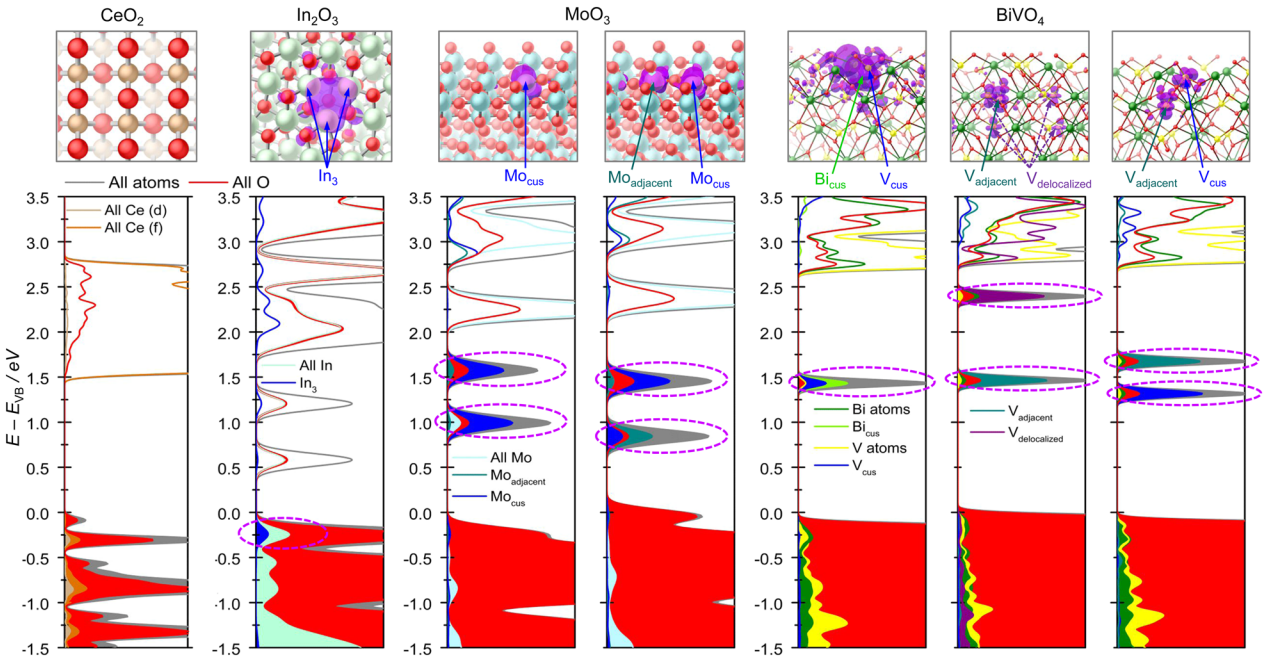

FIG. 4. Electron localization in the defective reducible oxide surfaces from left to right: $CeO_2(100)$, $In_2O_3(111)$, α-$MoO_3(010)$, and $BiVO_4(001)$. Top: structure and spatial electron density localization viewed from the top (CeO_2, In_2O_3) and side (MoO_3, $BiVO_4$). Bottom: atom-resolved Density of States (DOS) of the oxygen deficient surface (aligned vs the valence band maximum; filled colors represent occupied electronic states). Vacancy-induced excess electronic density is shown in magenta and encircled in the DOS; In_3 are the 3 In atoms surrounding the vacancy; M_{cus} are the coordinatively unsaturated metal sites, i.e., the metal sites that have lost an O coordination.

intragap state was observed and hopping conduction via small polaronic carriers would be expected.[35,92] Apart from the electronic conductivity, also the ionic conductivity is expected to increase through O vacancy migration in $BiVO_4$ bulk due to the low transition barriers for consecutive forming and breaking of V–O–V bonds.[36,92]

Those different geometries and electronic configurations have a large impact not only on the conductive properties but also on the catalytic activity. For example, such an extended delocalized charge state due to oxygen vacancies at the surface has also been found for WO_3 and is predicted to enhance the surface reactivity by promoting the formation of intermediate radical species at the surface.[173]

VII. HIGH-THROUGHPUT SCREENING

The search for new materials relies on extensive computation of the main properties in different crystalline materials. The realization that databases act as the starting point for these searches prompts the FAIR[174] principles of Findability, Accessibility, Interoperability, and Reusability to ensure a more ergonomic design. The Materials Genome database is a good example of a practical implementation.[14,21,175] Algorithms faced with a large candidate pool usually start by filtering out desired properties based on lower level theory.[23] This allows for a fast comparison of structural and electronic properties of a large set of different materials. Then, more specific filters are applied to this dataset, targeting particular properties, such as bandgaps or valence band levels.[17,20] In doing so, the number of potential materials is reduced, and in a next step, the desired properties are calculated at a higher level of theory for a smaller set of compounds. In this way, the structures can be employed for fast materials screening.[14–16,24] This is a great advance in the search for new materials, but in light of our studies, some subtleties, such as the role of defects and defect states, are only starting to be included.[24]

Our results for the oxides described above that can be consulted in the ioChem-BD database[168,176–180] show that vacancies can completely change the electronic structure, even for simple binary oxides. In particular, those defects which allow for quasi-degenerate states may be interesting for the desired applications and should therefore be carefully checked. They typically induce cations to show multiple redox pairs, configurations, or dynamicity, among other effects that might be amplified in high-entropy oxides.[181]

All these aspects should be included as filters in the new generation of screening engines in order to reduce the number of false positives, as proposed in Fig. 5: if the pristine material fulfills a given property at a particular level of the screening process, it should not be immediately accepted. Instead, the thermodynamical feasibility to form a vacancy has to be tested (considering a supercell). This defective structure then re-enter the funnel. Then, the possibility of a wide configurational space (many structures) or the formation of new bonds within the solid has to be checked, as it may introduce large differences in the material's properties. Finally, some metal centers may present multiple oxidation states and therefore lead to several possible electronic configurations, which have to

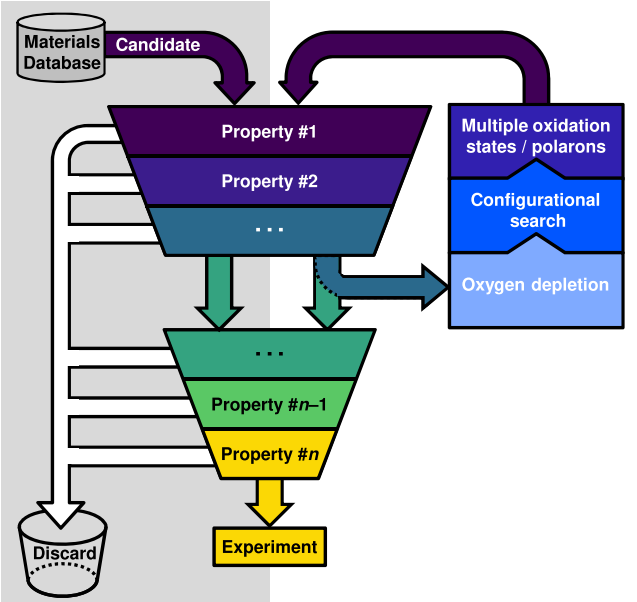

FIG. 5. Rational design of materials from large FAIR databases. In the traditional procedure (gray background), the material candidates are tested to fulfill a series of properties. Otherwise, they are discarded. The battery of tests goes from simple and cheap evaluations (upper block) to stricter techniques (lower block). To refine candidates and avoid false positives, the materials can be modified to match closely their experimental behavior just after the first battery of screening: by removing oxygen atoms, thus generating vacancies and defects, and by testing different configurations, oxidation states, and polarons.

be accounted for. Of course, the location of this new constraint in the list of filters needs to be evaluated with care. Typically, the funnel structure is built so that the larger number of structures are evaluated at a cheaper computational cost. Therefore, the particular location of our new filter will require to take into consideration the computational level needed and the number of configurations to be assessed.

VIII. CONCLUSIONS

Oxygen vacancies are ubiquitous in oxides, in part because of the thermal treatment employed in their synthesis. Traditionally, the residual electrons left by the O defect were assigned either to the vacancy site, to the metal cations (if those were reducible), or they delocalized in the case of a metallic oxide. In this perspective, by contextualizing a few examples from our group, we demonstrated how this picture is exceedingly simple. For instance, some surfaces are intrinsically defective and do not lead to the formation of electron centers. This is the case for some of the massive surface reconstructions that regulate the surface as with CeO_2 (100). The ultimate consequence of the lack of half of the atoms is that (i) the diffusion barrier of the remaining O atoms substantially decreases and (ii) several surface termination patterns coexist, resulting in a large stabilization due to configurational entropy. The most stable In_2O_3 surface, (111), exhibits a pattern where only some of the oxygen atoms can be removed preferentially, leaving spatially resolved isolated centers. Upon vacancy formation, the excess electrons are partially delocalized between three vacancy-surrounding In cations. In other systems, such as MoO_3, the cation can attain more than one oxidation state easily. The corresponding vacancy defect has two quasi-degenerate energy states that interconvert through polaron dynamics. A final observation regards more complex structures, such as $BiVO_4$. There, the vacancy can present two different geometries with the formation of a V–O–V bridging unit. As such, it can adapt to different electronic configurations, in which the excess electrons may localize on different V centers or instead delocalize in a two-dimensional extended charge state. The flexibility of the geometry and the redox character of both metals explains the versatility of vacancy structures in these ternary oxide materials.

In summary, the most common defect in oxides, the oxygen vacancy, presents a wide variety of behaviors that affect their electronic structure. In many cases, several near-degenerate electronic structures are needed to fully model the defect state. Even symmetric configurations have been found to break their symmetry under polaron interactions. Therefore, the rational design of new materials via high-throughput screening should also consider structures with one or more vacancies, the possibility of reconstruction, and that some constituents may adopt more than one oxidation state. Thus, any survey of reactivity and physical properties of reducible metal oxides, such as the ones discussed here, will require a wide sampling of the various cationic oxidation states and their locations. This aspect is often still overlooked in contemporary materials screening but will prove to be imperative in order to catch false positives and improve the accuracy of future predictions.

ACKNOWLEDGMENTS

The authors acknowledge the MCIU/AEI/ERDF-EU RTI2018-101394-B-I00, MINECO BES-2016-076361, and AGAUR 2017-SGR-90 projects for financial support, as well as the Barcelona Supercomputing Center (BSC-RES) for providing generous computer resources.

REFERENCES

[1] P. A. Cox, *Transition Metal Oxides: An Introduction to Their Electronic Structure and Properties*, International Series of Monographs on Chemistry (OUP, Oxford, 2010).
[2] V. E. Henrich and P. A. Cox, *The Surface Science of Metal Oxides* (Cambridge University Press, 1996).
[3] A. Fujishima and K. Honda, "Electrochemical photolysis of water at a semiconductor electrode," Nature **238**, 37–38 (1972).
[4] G. Pacchioni, "Oxygen vacancy: The invisible agent on oxide surfaces," ChemPhysChem **4**, 1041–1047 (2003).
[5] M. V. Ganduglia-Pirovano, A. Hofmann, and J. Sauer, "Oxygen vacancies in transition metal and rare earth oxides: Current state of understanding and remaining challenges," Surf. Sci. Rep. **62**, 219–270 (2007).
[6] G. Wang, Y. Ling, and Y. Li, "Oxygen-deficient metal oxide nanostructures for photoelectrochemical water oxidation and other applications," Nanoscale **4**, 6682–6691 (2012).
[7] Z. Wang, X. Mao, P. Chen, M. Xiao, S. A. Monny, S. Wang, M. Konarova, A. Du, and L. Wang, "Understanding the roles of oxygen vacancies in hematite-based photoelectrochemical processes," Angew. Chem. **131**, 1042–1046 (2019).

[8]N. W. Ashcroft and N. D. Mermin, in *Solid State Physics* (Brooks/Cole Cengage Learning, 1976), Chap. 30.
[9]A. P. Amrute, Z. Łodziana, H. Schreyer, C. Weidenthaler, and F. Schüth, "High-surface-area corundum by mechanochemically induced phase transformation of boehmite," Science **366**, 485–489 (2019).
[10]J. S. A. Carneiro, J. Williams, A. Gryko, L. P. Herrera, and E. Nikolla, "Embracing complexity of catalytic structures: A viewpoint on synthesis of non-stoichiometric mixed metal oxides for catalysis," ACS Catal. **10**, 516–527 (2020).
[11]M. T. Greiner, L. Chai, M. G. Helander, W. M. Tang, and Z. H. Lu, "Transition metal oxide work functions: The influence of cation oxidation state and oxygen vacancies," Adv. Funct. Mater. **22**, 4557–4568 (2012).
[12]F. Studt, F. Abild-Pedersen, H. A. Hansen, I. C. Man, J. Rossmeisl, and T. Bligaard, "Volcano relation for the deacon process over transition-metal oxides," ChemCatChem **2**, 98–102 (2010).
[13]D. W. Davies, C. N. Savory, J. M. Frost, O. David, B. J. Morgan, and A. Walsh, "Descriptors for electron and hole charge carriers in metal oxides," J. Phys. Chem. Lett. **11**, 438–444 (2020).
[14]A. Jain, S. P. Ong, G. Hautier, W. Chen, W. D. Richards, S. Dacek, S. Cholia, D. Gunter, D. Skinner, G. Ceder *et al.*, "Commentary: The materials project: A materials genome approach to accelerating materials innovation," APL Mater. **1**, 011002 (2013).
[15]D. D. Landis, J. S. Hummelshoj, S. Nestorov, J. Greeley, M. Dulak, T. Bligaard, J. K. Norskov, and K. W. Jacobsen, "The computational materials repository," Comput. Sci. Eng. **14**, 51 (2012).
[16]I. E. Castelli, D. D. Landis, K. S. Thygesen, S. Dahl, I. Chorkendorff, T. F. Jaramillo, and K. W. Jacobsen, "New cubic perovskites for one- and two-photon water splitting using the computational materials repository," Energy Environ. Sci. **5**, 9034–9043 (2012).
[17]I. E. Castelli, T. Olsen, S. Datta, D. D. Landis, S. Dahl, K. S. Thygesen, and K. W. Jacobsen, "Computational screening of perovskite metal oxides for optimal solar light capture," Energy Environ. Sci. **5**, 5814–5819 (2012).
[18]J. Lee, A. Seko, K. Shitara, K. Nakayama, and I. Tanaka, "Prediction model of band gap for inorganic compounds by combination of density functional theory calculations and machine learning techniques," Phys. Rev. B **93**, 115104 (2016).
[19]J. J. Plata Ramos, J. Amaya-Suarez, S. Cuesta-López, A. Márquez, and J. Fernández Sanz, "Photo-sensitizing thin-film ferroelectric oxides using materials databases and high-throughput calculations," J. Mater. Chem. A **7**, 27323–27333 (2019).
[20]Q. Yan, J. Yu, S. K. Suram, L. Zhou, A. Shinde, P. F. Newhouse, W. Chen, G. Li, K. A. Persson, J. M. Gregoire *et al.*, "Solar fuels photoanode materials discovery by integrating high-throughput theory and experiment," Proc. Natl. Acad. Sci. U. S. A. **114**, 3040–3043 (2017).
[21]J. J. de Pablo, B. Jones, C. L. Kovacs, V. Ozolins, and A. P. Ramirez, "The materials genome initiative, the interplay of experiment, theory and computation," Curr. Opin. Solid State Mater. Sci. **18**, 99–117 (2014).
[22]D. Broberg, B. Medasani, N. E. R. Zimmermann, G. Yu, A. Canning, M. Haranczyk, M. Asta, and G. Hautier, "PyCDT: A python toolkit for modeling point defects in semiconductors and insulators," Comput. Phys. Commun. **226**, 165–179 (2018).
[23]C. Bo, F. Maseras, and N. López, "The role of computational results databases in accelerating the discovery of catalysts," Nat. Catal. **1**, 809–810 (2018).
[24]W. Chen, J. George, J. B. Varley, G.-M. Rignanese, and G. Hautier, "High-throughput computational discovery of $In_2Mn_2O_7$ as a high Curie temperature ferromagnetic semiconductor for spintronics," npj Comput. Mater. **5**, 72 (2019).
[25]A. Ruiz Puigdollers, P. Schlexer, S. Tosoni, and G. Pacchioni, "Increasing oxide reducibility: The role of metal/oxide interfaces in The formation of oxygen vacancies," ACS Catal. **7**, 6493–6513 (2017).
[26]J. Carrasco, N. López, and F. Illas, "First principles analysis of the stability and diffusion of oxygen vacancies in metal oxides," Phys. Rev. Lett. **93**, 225502 (2004).
[27]J. Carrasco, N. Lopez, F. Illas, and H.-J. Freund, "Bulk and surface oxygen vacancy formation and diffusion in single crystals, ultrathin films, and metal grown oxide structures," J. Chem. Phys. **125**, 074711 (2006).
[28]M. Boero, A. Pasquarello, J. Sarnthein, and R. Car, "Structure and hyperfine parameters of E'_1 centers in α-quartz and in vitreous SiO_2," Phys. Rev. Lett. **78**, 887 (1997).
[29]G. Pacchioni and G. Ieranò, "Computed optical absorption and photoluminescence spectra of neutral oxygen vacancies in α-quartz," Phys. Rev. Lett. **79**, 753 (1997).
[30]M. Boero, A. Oshiyama, and P. L. Silvestrelli, "E′ centers in silicon dioxide: First-principles molecular dynamics studies," Mod. Phys. Lett. B **18**, 707–724 (2004).
[31]Y. Yue, Y. Song, and X. Zuo, "First principles study of oxygen vacancy defects in amorphous SiO_2," AIP Adv. **7**, 015309 (2017).
[32]A. Walsh, A. A. Sokol, J. Buckeridge, D. O. Scanlon, and C. R. A. Catlow, "Oxidation states and ionicity," Nat. Mater. **17**, 958–964 (2018).
[33]J. T. Devreese, "Polarons," in *Encyclopedia of Applied Physics* (Wiley-VCH Publishers, Inc., 1996), Vol. 14, pp. 383–409.
[34]E. Pastor, J. S. Park, L. Steier, S. Kim, M. Grätzel, J. R. Durrant, A. Walsh, and A. A. Bakulin, "*In situ* observation of picosecond polaron self-localisation in α-Fe_2O_3 photoelectrochemical cells," Nat. Commun. **10**, 1–7 (2019).
[35]H. Seo, Y. Ping, and G. Galli, "Role of point defects in enhancing the conductivity of $BiVO_4$," Chem. Mater. **30**, 7793–7802 (2018).
[36]X. Yang, A. J. Fernández-Carrión, J. Wang, F. Porcher, F. Fayon, M. Allix, and X. Kuang, "Cooperative mechanisms of oxygen vacancy stabilization and migration in the isolated tetrahedral anion Scheelite structure," Nat. Commun. **9**, 4484 (2018).
[37]U. Diebold, "The surface science of titanium dioxide," Surf. Sci. Rep. **48**, 53–229 (2003).
[38]F. De Angelis, C. Di Valentin, S. Fantacci, A. Vittadini, and A. Selloni, "Theoretical studies on anatase and less common TiO_2 phases: Bulk, surfaces, and nanomaterials," Chem. Rev. **114**, 9708–9753 (2014).
[39]A. G. Thomas, W. R. Flavell, A. K. Mallick, A. R. Kumarasinghe, D. Tsoutsou, N. Khan, C. Chatwin, S. Rayner, G. C. Smith, R. L. Stockbauer *et al.*, "Comparison of the electronic structure of anatase and rutile TiO_2 single-crystal surfaces using resonant photoemission and x-ray absorption spectroscopy," Phys. Rev. B **75**, 035105 (2007).
[40]C. Di Valentin and A. Selloni, "Bulk and surface polarons in photoexcited anatase TiO_2," J. Phys. Chem. Lett. **2**, 2223–2228 (2011).
[41]W.-J. Yin, B. Wen, C. Zhou, A. Selloni, and L.-M. Liu, "Excess electrons in reduced rutile and anatase TiO_2," Surf. Sci. Rep. **73**, 58–82 (2018).
[42]P. M. Kowalski, M. F. Camellone, N. N. Nair, B. Meyer, and D. Marx, "Charge localization dynamics induced by oxygen vacancies on the TiO_2(110) surface," Phys. Rev. Lett. **105**, 146405 (2010).
[43]S. Selcuk and A. Selloni, "Facet-dependent trapping and dynamics of excess electrons at anatase TiO_2 surfaces and aqueous interfaces," Nat. Mater. **15**, 1107 (2016).
[44]A. Magnéli, "The crystal structures of Mo_9O_{26} (β'-molybdenum oxide) and Mo_8O_{23} (β-molybdenum oxide)," Acta Chem. Scand. **2**, 501–517 (1948).
[45]M. Moser, I. Czekaj, N. López, and J. Pérez-Ramírez, "The virtue of defects: Stable bromine production by catalytic oxidation of hydrogen bromide on titanium oxide," Angew. Chem., Int. Ed. **53**, 8628–8633 (2014).
[46]M. Sachs, J.-S. Park, E. Pastor, A. Kafizas, A. A. Wilson, L. Francàs, S. Gul, M. Ling, C. Blackman, J. Yano *et al.*, "Effect of oxygen deficiency on the excited state kinetics of WO_3 and implications for photocatalysis," Chem. Sci. **10**, 5667–5677 (2019).
[47]M. Domaschke, X. Zhou, L. Wergen, S. Romeis, M. E. Miehlich, K. Meyer, W. Peukert, and P. Schmuki, "Magnéli-phases in anatase strongly promote cocatalyst-free photocatalytic hydrogen evolution," ACS Catal. **9**, 3627–3632 (2019).
[48]Y.-J. Lee, T. Lee, and A. Soon, "Phase stability diagrams of group 6 Magnéli oxides and their implications for photon-assisted applications," Chem. Mater. **31**, 4282–4290 (2019).

[49] N. Lopez, J. Gómez-Segura, R. P. Marín, and J. Perez-Ramirez, "Mechanism of HCl oxidation (Deacon process) over RuO_2," J. Catal. **255**, 29–39 (2008).
[50] A. Trovarelli and P. Fornasiero, *Catalytic Science Series*, 2nd ed. (Imperial College Press, London, 2013), Vol. 12, p. 888.
[51] C. Xu and X. Qu, "Cerium oxide nanoparticle: A remarkably versatile rare earth nanomaterial for biological applications," NPG Asia Mater. **6**, e90 (2014).
[52] M. Capdevila-Cortada, G. Vilé, D. Teschner, J. Pérez-Ramírez, and N. López, "Reactivity descriptors for ceria in catalysis," Appl. Catal., B **197**, 299–312 (2016).
[53] R. Bel Hadj Tahar, T. Ban, Y. Ohya, and Y. Takahashi, "Tin doped indium oxide thin films: Electrical properties," J. Appl. Phys. **83**, 2631–2645 (1998).
[54] O. Martin, A. J. Martín, C. Mondelli, S. Mitchell, T. F. Segawa, R. Hauert, C. Drouilly, D. Curulla-Ferré, and J. Pérez-Ramírez, "Indium oxide as a superior catalyst for methanol synthesis by CO_2 hydrogenation," Angew. Chem., Int. Ed. **55**, 6261–6265 (2016).
[55] I. Alves de Castro, R. S. Datta, J. Z. Ou, A. Castellanos-Gomez, S. Sriram, T. Daeneke, and K. Kalantar-Zadeh, "Molybdenum oxides–from fundamentals to functionality," Adv. Mater. **29**, 1701619 (2017).
[56] A. Kudo, K. Ueda, H. Kato, and I. Mikami, "Photocatalytic O_2 evolution under visible light irradiation on $BiVO_4$ in aqueous $AgNO_3$ solution," Catal. Lett. **53**, 229–230 (1998).
[57] I. D. Sharp, J. K. Cooper, F. M. Toma, and R. Buonsanti, "Bismuth vanadate as a platform for accelerating discovery and development of complex transition-metal oxide photoanodes," ACS Energy Lett. **2**, 139–150 (2017).
[58] P. Hohenberg and W. Kohn, "Inhomogeneous electron gas," Phys. Rev. **136**, B864 (1964).
[59] W. Kohn and L. J. Sham, "Self-consistent equations including exchange and correlation effects," Phys. Rev. **140**, A1133 (1965).
[60] K. Lejaeghere, G. Bihlmayer, T. Björkman, P. Blaha, S. Blügel, V. Blum, D. Caliste, I. E. Castelli, S. J. Clark, A. Dal Corso, S. de Gironcoli, T. Deutsch, J. K. Dewhurst, I. Di Marco, C. Draxl, M. Dułak, O. Eriksson, J. A. Flores-Livas, K. F. Garrity, L. Genovese, P. Giannozzi, M. Giantomassi, S. Goedecker, X. Gonze, O. Grånäs, E. K. U. Gross, A. Gulans, F. Gygi, D. R. Hamann, P. J. Hasnip, N. A. W. Holzwarth, D. Iuşan, D. B. Jochym, F. Jollet, D. Jones, G. Kresse, K. Koepernik, E. Küçükbenli, Y. O. Kvashnin, I. L. M. Locht, S. Lubeck, M. Marsman, N. Marzari, U. Nitzsche, L. Nordström, T. Ozaki, L. Paulatto, C. J. Pickard, W. Poelmans, M. I. J. Probert, K. Refson, M. Richter, G.-M. Rignanese, S. Saha, M. Scheffler, M. Schlipf, K. Schwarz, S. Sharma, F. Tavazza, P. Thunström, A. Tkatchenko, M. Torrent, D. Vanderbilt, M. J. van Setten, V. Van Speybroeck, J. M. Wills, J. R. Yates, G.-X. Zhang, and S. Cottenier, "Reproducibility in density functional theory calculations of solids," Science **351**, aad3000 (2016).
[61] J. P. Perdew and Y. Wang, "Accurate and simple analytic representation of the electron-gas correlation energy," Phys. Rev. B **45**, 13244 (1992).
[62] J. P. Perdew, K. Burke, and M. Ernzerhof, "Generalized gradient approximation made simple," Phys. Rev. Lett. **77**, 3865 (1996).
[63] Y. Zhang and W. Yang, "Comment on "Generalized gradient approximation made simple,"" Phys. Rev. Lett. **80**, 890 (1998).
[64] B. Hammer, L. B. Hansen, and J. K. Nørskov, "Improved adsorption energetics within density-functional theory using revised Perdew-Burke-Ernzerhof functionals," Phys. Rev. B **59**, 7413 (1999).
[65] J. P. Perdew, A. Ruzsinszky, G. I. Csonka, O. A. Vydrov, G. E. Scuseria, L. A. Constantin, X. Zhou, and K. Burke, "Restoring the density-gradient expansion for exchange in solids and surfaces," Phys. Rev. Lett. **100**, 136406 (2008).
[66] J. Wellendorff, T. L. Silbaugh, D. Garcia-Pintos, J. K. Nørskov, T. Bligaard, F. Studt, and C. T. Campbell, "A benchmark database for adsorption bond energies to transition metal surfaces and comparison to selected DFT functionals," Surf. Sci. **640**, 36–44 (2015).
[67] J. P. Perdew and K. Schmidt, "Jacob's ladder of density functional approximations for the exchange-correlation energy," AIP Conf. Proc. **577**, 1 (2001).
[68] A. I. Liechtenstein, V. I. Anisimov, and J. Zaanen, "Density-functional theory and strong interactions: Orbital ordering in Mott-Hubbard insulators," Phys. Rev. B **52**, R5467 (1995).
[69] V. I. Anisimov, J. Zaanen, and O. K. Andersen, "Band theory and Mott insulators: Hubbard U instead of Stoner I," Phys. Rev. B **44**, 943 (1991).
[70] J. Hubbard, "Electron correlations in narrow energy bands," Proc. R. Soc. London, Ser. A **276**, 238–257 (1963).
[71] H. J. Kulik and N. Marzari, "Accurate potential energy surfaces with a DFT+U(R) approach," J. Chem. Phys. **135**, 194105 (2011).
[72] M. Aykol and C. Wolverton, "Local environment dependent GGA+U method for accurate thermochemistry of transition metal compounds," Phys. Rev. B **90**, 115105 (2014).
[73] N. R. Mathiesen, S. Yang, J. M. García-Lastra, T. Vegge, and D. J. Siegel, "Charge transport in alkali-metal superoxides: A systematic first-principles study," Chem. Mater. **31**, 9156–9167 (2019).
[74] S. L. Dudarev, G. A. Botton, S. Y. Savrasov, C. J. Humphreys, and A. P. Sutton, "Electron-energy-loss spectra and the structural stability of nickel oxide: An LSDA+U study," Phys. Rev. B **57**, 1505–1509 (1998).
[75] M. Cococcioni and S. de Gironcoli, "Linear response approach to the calculation of the effective interaction parameters in the LDA+U method," Phys. Rev. B **71**, 035105 (2005).
[76] M. Capdevila-Cortada, Z. Łodziana, and N. López, "Performance of DFT+U approaches in the study of catalytic materials," ACS Catal. **6**, 8370–8379 (2016).
[77] H. J. Kulik, M. Cococcioni, D. A. Scherlis, and N. Marzari, "Density functional theory in transition-metal chemistry: A self-consistent Hubbard U approach," Phys. Rev. Lett. **97**, 103001 (2006).
[78] J. L. F. Da Silva, M. V. Ganduglia-Pirovano, J. Sauer, V. Bayer, and G. Kresse, "Hybrid functionals applied to rare-earth oxides: The example of ceria," Phys. Rev. B **75**, 45121 (2007).
[79] M. Nolan, S. C. Parker, and G. W. Watson, "The electronic structure of oxygen vacancy defects at the low index surfaces of ceria," Surf. Sci. **595**, 223–232 (2005).
[80] J. Paier, "Hybrid density functionals applied to complex solid catalysts: Successes, limitations, and prospects," Catal. Lett. **146**, 861–885 (2016).
[81] M. Rellán-Piñeiro and N. López, "One oxygen vacancy, two charge states: Characterization of reduced α-MoO_3 (010) through theoretical methods," J. Phys. Chem. Lett. **9**, 2568–2573 (2018).
[82] J. P. Perdew, M. Ernzerhof, and K. Burke, "Rationale for mixing exact exchange with density functional approximations," J. Chem. Phys. **105**, 9982–9985 (1996).
[83] J. Heyd and G. E. Scuseria, "Assessment and validation of a screened Coulomb hybrid density functional," J. Chem. Phys. **120**, 7274–7280 (2004).
[84] A. Alkauskas, P. Broqvist, F. Devynck, and A. Pasquarello, "Band offsets at semiconductor-oxide interfaces from hybrid density-functional calculations," Phys. Rev. Lett. **101**, 106802 (2008).
[85] Z. D. Pozun and G. Henkelman, "Hybrid density functional theory band structure engineering in hematite," J. Chem. Phys. **134**, 224706 (2011).
[86] K. E. Kweon, G. S. Hwang, J. Kim, S. Kim, and S. Kim, "Electron small polarons and their transport in bismuth vanadate: A first principles study," Phys. Chem. Chem. Phys. **17**, 256–260 (2015).
[87] F. S. Hegner, I. Herraiz-Cardona, D. Cardenas-Morcoso, N. López, J.-R. Galán-Mascarós, and S. Gimenez, "Cobalt hexacyanoferrate on $BiVO_4$ photoanodes for robust water splitting," ACS Appl. Mater. Interfaces **9**, 37671–37681 (2017).
[88] P. Broqvist, A. Alkauskas, and A. Pasquarello, "A hybrid functional scheme for defect levels and band alignments at semiconductor–oxide interfaces," Phys. Status Solidi A **207**, 270–276 (2010).
[89] A. Alkauskas, P. Broqvist, and A. Pasquarello, "Defect levels through hybrid density functionals: Insights and applications," Phys. Status Solidi B **248**, 775–789 (2011).
[90] J. H. Skone, M. Govoni, and G. Galli, "Self-consistent hybrid functional for condensed systems," Phys. Rev. B **89**, 195112 (2014).
[91] J. He and C. Franchini, "Assessing the performance of self-consistent hybrid functional for band gap calculation in oxide semiconductors," J. Phys.: Condens. Matter **29**, 454004 (2017).

[92]F. S. Hegner, D. Forrer, J. R. Galán-Mascaros, N. López, and A. Selloni, "The versatile nature of oxygen vacancies in bismuth vanadate bulk and (001) surface," J. Phys. Chem. Lett. **10**, 6672–6678 (2019).
[93]D. Du, M. J. Wolf, K. Hermansson, and P. Broqvist, "Screened hybrid functionals applied to ceria: Effect of Fock exchange," Phys. Rev. B **97**, 235203 (2018).
[94]G. Strinati, "Application of the Green's functions method to the study of the optical properties of semiconductors," Riv. Nuovo Cimento **11**, 1–86 (1988).
[95]S. Refaely-Abramson, D. Y. Qiu, S. G. Louie, and J. B. Neaton, "Defect-induced modification of low-lying excitons and valley selectivity in monolayer transition metal dichalcogenides," Phys. Rev. Lett. **121**, 167402 (2018).
[96]W. Chen and A. Pasquarello, "Accuracy of GW for calculating defect energy levels in solids," Phys. Rev. B **96**, 020101 (2017).
[97]F. Goubin, X. Rocquefelte, M. H. Whangbo, Y. Montardi, R. Brec, and S. Jobic, "Experimental and theoretical characterization of the optical properties of CeO_2, $SrCeO_3$, and Sr_2CeO_4 containing Ce^{4+} (f^0) ions," Chem. Mater. **16**, 662–669 (2004).
[98]S. A. Ansari, M. M. Khan, M. O. Ansari, S. Kalathil, J. Lee, and M. H. Cho, "Band gap engineering of CeO_2 nanostructure using an electrochemically active biofilm for visible light applications," RSC Adv. **4**, 16782–16791 (2014).
[99]A. Trovarelli, "Catalytic properties of ceria and CeO_2-containing materials," Catal. Rev.-Sci. Eng. **38**, 439–520 (1996).
[100]A. P. Amrute, C. Mondelli, M. Moser, G. Novell-Leruth, N. López, D. Rosenthal, R. Farra, M. E. Schuster, D. Teschner, T. Schmidt, and J. Pérez-Ramírez, "Performance, structure, and mechanism of CeO_2 in HCl oxidation to Cl_2," J. Catal. **286**, 287–297 (2012).
[101]M. Scharfe, M. Capdevila-Cortada, V. A. Kondratenko, E. V. Kondratenko, S. Colussi, A. Trovarelli, N. López, and J. Pérez-Ramírez, "Mechanism of ethylene oxychlorination on ceria," ACS Catal. **8**, 2651–2663 (2018).
[102]B. Puértolas, M. Rellán-Piñeiro, J. L. Núñez-Rico, A. P. Amrute, A. Vidal-Ferran, N. López, J. Pérez-Ramírez, and S. Wershofen, "Mechanistic insights into the ceria-catalyzed synthesis of carbamates as polyurethane precursors," ACS Catal. **9**, 7708–7720 (2019).
[103]V. Paunović, M. Rellán-Piñeiro, N. López, and J. Pérez-Ramírez, "Activity differences of rutile and anatase TiO_2 polymorphs in catalytic HBr oxidation for bromine-mediated upgrading of natural gas" (submitted) (2020).
[104]C. Yang, X. Yu, S. Heißler, A. Nefedov, S. Colussi, J. Llorca, A. Trovarelli, Y. Wang, and C. Wöll, "Surface faceting and reconstruction of ceria nanoparticles," Angew. Chem., Int. Ed. **56**, 375–379 (2017).
[105]S. Torbrügge, M. Reichling, A. Ishiyama, S. Morita, and Ó. Custance, "Evidence of subsurface oxygen vacancy ordering on reduced CeO_2(111)," Phys. Rev. Lett. **99**, 056101 (2007).
[106]M. V. Ganduglia-Pirovano, J. L. F. Da Silva, and J. Sauer, "Density-functional calculations of the structure of near-surface oxygen vacancies and electron localization on CeO_2(111)," Phys. Rev. Lett. **102**, 026101 (2009).
[107]J.-F. Jerratsch, X. Shao, N. Nilius, H.-J. Freund, C. Popa, M. V. Ganduglia-Pirovano, A. M. Burow, and J. Sauer, "Electron localization in defective ceria films: A study with scanning-tunneling microscopy and density-functional theory," Phys. Rev. Lett. **106**, 246801 (2011).
[108]F. Esch, S. Fabris, L. Zhou, T. Montini, C. Africh, P. Fornasiero, G. Comelli, and R. Rosei, "Electron localization determines defect formation on ceria substrates," Science **309**, 752–755 (2005).
[109]G. Carchini, M. García-Melchor, Z. Łodziana, and N. López, "Understanding and tuning the intrinsic hydrophobicity of rare-earth oxides: A DFT+U study," ACS Appl. Mater. Interfaces **8**, 152–160 (2016).
[110]The surface in question bears a net charge and dipole moment perpendicular to the repeating unit cell.
[111]P. W. Tasker, "The stability of ionic crystal surfaces," J. Phys. C: Solid State Phys. **12**, 4977 (1979).
[112]M. Capdevila-Cortada and N. López, "Entropic contributions enhance polarity compensation for CeO_2 (100) surfaces," Nat. Mater. **16**, 328–334 (2017).
[113]M. Bugnet, S. H. Overbury, Z. L. Wu, and T. Epicier, "Direct visualization and control of atomic mobility at {100} surfaces of ceria in the environmental transmission electron microscope," Nano Lett. **17**, 7652–7658 (2017).
[114]N. Daelman, M. Capdevila-Cortada, and N. López, "Dynamic charge and oxidation state of Pt/CeO_2 single-atom catalysts," Nat. Mater. **18**, 1215–1221 (2019).
[115]D. Albani, M. Capdevila-Cortada, G. Vilé, S. Mitchell, O. Martin, N. López, and J. Pérez-Ramírez, "Semihydrogenation of acetylene on indium oxide: Proposed single-ensemble catalysis," Angew. Chem., Int. Ed. **56**, 10755–10760 (2017).
[116]T. Koida, H. Fujiwara, and M. Kondo, "Hydrogen-doped In_2O_3 as high-mobility transparent conductive oxide," Jpn. J. Appl. Phys., Part 2 **46**, L685–L687 (2007).
[117]A. Walsh and C. R. A. Catlow, "Structure, stability and work functions of the low index surfaces of pure indium oxide and Sn-doped indium oxide (ITO) from density functional theory," J. Mater. Chem. **20**, 10438–10444 (2010).
[118]M. Chen, J. Xu, Y.-M. Liu, Y. Cao, H.-Y. He, and J.-H. Zhuang, "Supported indium oxide as novel efficient catalysts for dehydrogenation of propane with carbon dioxide," Appl. Catal., A **377**, 35–41 (2010).
[119]M. S. Frei, M. Capdevila-Cortada, R. García-Muelas, C. Mondelli, N. López, J. A. Stewart, D. C. Ferré, and J. Pérez-Ramírez, "Mechanism and microkinetics of methanol synthesis via CO_2 hydrogenation on indium oxide," J. Catal. **361**, 313–321 (2018).
[120]M. S. Frei, C. Mondelli, A. Cesarini, F. Krumeich, R. Hauert, J. A. Stewart, D. Curulla Ferre, and J. Pérez-Ramírez, "Role of zirconia carrier on indium oxide-catalyzed CO_2 hydrogenation to methanol," ACS Catal. **10**, 1133–1145 (2020).
[121]K. Metals, Strategic metals market price; accessed 31 October 2019, https://www.kitco.com/strategic-metals/.
[122]M. Marezio, "Refinement of the crystal structure of In_2O_3 at two wavelengths," Acta Crystallogr. **20**, 723–728 (1966).
[123]C. T. Prewitt, R. D. Shannon, D. B. Rogers, and A. W. Sleight, "The C rare earth oxide-corundum transition and crystal chemistry of oxides having the corundum structure," Inorg. Chem. **8**, 1985–1993 (1969).
[124]T. Koida, H. Shibata, M. Kondo, K. Tsutsumi, A. Sakaguchi, M. Suzuki, and H. Fujiwara, "Correlation between oxygen stoichiometry, structure, and opto-electrical properties in amorphous In_2O_3: H films," J. Appl. Phys. **111**, 063721 (2012).
[125]S. Geller, J. A. Cape, R. W. Grant, and G. P. Espinosa, "Distortion in the crystal structure of α-Mn_2O_3," Phys. Lett. A **24**, 369–371 (1967).
[126]K. H. L. Zhang, A. Walsh, C. R. A. Catlow, V. K. Lazarov, and R. G. Egdell, "Surface energies control the self-organization of oriented In_2O_3 nanostructures on cubic zirconia," Nano Lett. **10**, 3740–3746 (2010).
[127]K. H. L. Zhang, R. G. Egdell, F. Offi, S. Iacobucci, L. Petaccia, S. Gorovikov, and P. D. C. King, "Microscopic origin of electron accumulation in In_2O_3," Phys. Rev. Lett. **110**, 056803 (2013).
[128]M. Wagner, S. Seiler, B. Meyer, L. A. Boatner, M. Schmid, and U. Diebold, "Reducing the In_2O_3 (111) surface results in ordered indium adatoms," Adv. Mater. Interfaces **1**, 1400289 (2014).
[129]T. Bielz, H. Lorenz, W. Jochum, R. Kaindl, F. Klauser, B. Klotzer, and S. Penner, "Hydrogen on In_2O_3: Reducibility, bonding, defect formation, and reactivity," J. Phys. Chem. C **114**, 9022–9029 (2010).
[130]A. Walsh, "Surface oxygen vacancy origin of electron accumulation in indium oxide," Appl. Phys. Lett. **98**, 261910 (2011).
[131]L. He, T. E. Wood, B. Wu, Y. Dong, L. B. Hoch, L. M. Reyes, D. Wang, C. Kübel, C. Qian, J. Jia, K. Liao, P. G. O'Brien, A. Sandhel, J. Y. Y. Loh, P. Szymanski, N. P. Kherani, T. C. Sum, C. A. Mims, and G. A. Ozin, "Spatial separation of charge carriers in $In_2O_{3-x}(OH)_y$ nanocrystal superstructures for enhanced gas-phase photocatalytic activity," ACS Nano **10**, 5578–5586 (2016).
[132]K. K. Ghuman, L. B. Hoch, P. Szymanski, J. Y. Y. Loh, N. P. Kherani, M. A. El-Sayed, G. A. Ozin, and C. V. Singh, "Photoexcited surface frustrated Lewis pairs for heterogeneous photocatalytic CO_2 reduction," J. Am. Chem. Soc. **138**, 1206–1214 (2016).
[133]M. S. Frei, C. Mondelli, R. García-Muelas, K. S. Kley, B. Puértolas, N. López, O. V. Safonova, J. A. Stewart, D. C. Ferré, and J. Pérez-Ramírez, "Atomic-scale engineering of indium oxide promotion by palladium for methanol production via CO_2 hydrogenation," Nat. Commun. **10**, 3377 (2019).

[134]M. G. O'Brien, A. M. Beale, S. D. M. Jacques, T. Buslaps, V. Honkimaki, and B. M. Weckhuysen, "On the active oxygen in bulk MoO_3 during the anaerobic dehydrogenation of methanol," J. Phys. Chem. C **113**, 4890–4897 (2009).
[135]A. M. Bahmanpour, A. Hoadley, and A. Tanksale, "Critical review and exergy analysis of formaldehyde production processes," Rev. Chem. Eng. **30**, 583–604 (2014).
[136]M. Rellán-Piñeiro and N. López, "The active molybdenum oxide phase in the methanol oxidation to formaldehyde (Formox process): A DFT study," ChemSusChem **8**, 2231–2239 (2015).
[137]T. Choksi and J. Greeley, "Partial oxidation of methanol on MoO_3 (010): A DFT and microkinetic study," ACS Catal. **6**, 7260–7277 (2016).
[138]M. Shetty, K. Murugappan, T. Prasomsri, W. H. Green, and Y. Roman-Leshkov, "Reactivity and stability investigation of supported molybdenum oxide catalysts for the hydrodeoxygenation (HDO) of m-cresol," J. Catal. **331**, 86–97 (2015).
[139]V. Zacharopoulou, E. S. Vasiliadou, and A. A. Lemonidou, "One-step propylene formation from bio-glycerol over molybdena-based catalysts," Green Chem. **17**, 903–912 (2015).
[140]M. Shetty, B. Buesser, Y. Román-Leshkov, and W. H. Green, "Computational investigation on hydrodeoxygenation (HDO) of acetone to propylene on α-MoO_3(010) surface," J. Phys. Chem. C **121**, 17848–17855 (2017).
[141]M. Rellán-Piñeiro and N. López, "A coupled density functional theory–microkinetic modeling for the hydrodeoxygenation of glycerol to propylene on MoO_3," ACS Sustainable Chem. Eng. **6**, 16169–16178 (2018).
[142]S. K. Deb, "Physical properties of a transition metal oxide: Optical and photoelectric properties of single crystal and thin film molybdenum trioxide," Proc. R. Soc. London, Ser. A **304**, 211–231 (1968).
[143]R. B. Dzhanelidze, I. M. Purstelazde, L. S. Khitarishvili, R. I. Chikovani, and A. L. Shkolnij, "Some optical and photoelectric properties of MoO_3," Phys. Solid State **7**, 2082–2083 (1966).
[144]A. Bouzidi, N. Benramdane, H. Tabet-Derraz, C. Mathieu, B. Khelifa, and R. Desfeux, "Effect of substrate temperature on the structural and optical properties of MoO_3 thin films prepared by spray pyrolysis technique," Mater. Sci. Eng., B **97**, 5–8 (2003).
[145]M. Kröger, S. Hamwi, J. Meyer, T. Riedl, W. Kowalsky, and A. Kahn, "P-type doping of organic wide band gap materials by transition metal oxides: A case-study on molybdenum trioxide," Org. Electron. **10**, 932–938 (2009).
[146]T. S. Sian and G. B. Reddy, "Optical, structural and photoelectron spectroscopic studies on amorphous and crystalline molybdenum oxide thin films," Sol. Energy Mater. Sol. Cells **82**, 375–386 (2004).
[147]H. S. Kim, J. B. Cook, H. Lin, J. S. Ko, S. H. Tolbert, V. Ozolins, and B. Dunn, "Oxygen vacancies enhance pseudocapacitive charge storage properties of MoO_{3-x}," Nat. Mater. **16**, 454–460 (2017).
[148]M. Dieterle, G. Weinberg, and G. Mestl, "Raman spectroscopy of molybdenum oxides. Part I. Structural characterization of oxygen defects in MoO_{3-x} by DR UV/VIS, Raman spectroscopy and x-ray diffraction," Phys. Chem. Chem. Phys. **4**, 812–821 (2002).
[149]V. Zacharopoulou, E. S. Vasiliadou, and A. A. Lemonidou, "Exploring the reaction pathways of bioglycerol hydrodeoxygenation to propene over molybdena-based catalysts," ChemSusChem **11**, 264–275 (2018).
[150]H. Ding, H. Lin, B. Sadigh, F. Zhou, V. Ozoliņš, and M. Asta, "Computational investigation of electron small polarons in α-MoO_3," J. Phys. Chem. C **118**, 15565–15572 (2014).
[151]H. A. Tahini, X. Tan, S. N. Lou, J. Scott, R. Amal, Y. H. Ng, and S. C. Smith, "Mobile polaronic states in α-MoO_3: An *ab initio* investigation of the role of oxygen vacancies and alkali ions," ACS Appl. Mater. Interfaces **8**, 10911–10917 (2016).
[152]J. Carrasco, F. Illas, N. Lopez, E. Kotomin, Y. F. Zhukovskii, R. A. Evarestov, Y. A. Mastrikov, S. Piskunov, and J. Maier, "First-principles calculations of the atomic and electronic structure of f centers in the bulk and on the (001) surface of $SrTiO_3$," Phys. Rev. B **73**, 064106 (2006).
[153]Y.-Y. Pai, A. Tylan-Tyler, P. Irvin, and J. Levy, "Physics of $SrTiO_3$-based heterostructures and nanostructures: A review," Rep. Prog. Phys. **81**, 036503 (2018).
[154]A. Al-Zubi, G. Bihlmayer, and S. Blügel, "Electronic structure of oxygen-deficient $SrTiO_3$ and Sr_2TiO_4," Crystals **9**, 580 (2019).
[155]Y. Pihosh, I. Turkevych, K. Mawatari, J. Uemura, Y. Kazoe, S. Kosar, K. Makita, T. Sugaya, T. Matsui, D. Fujita *et al.*, "Photocatalytic generation of hydrogen by core-shell WO_3/$BiVO_4$ nanorods with ultimate water splitting efficiency," Sci. Rep. **5**, 11141 (2015).
[156]K. Tolod, S. Hernández, and N. Russo, "Recent advances in the $BiVO_4$ photocatalyst for sun-driven water oxidation: Top-performing photoanodes and scale-up challenges," Catalysts **7**, 13 (2017).
[157]A. J. Rettie, W. D. Chemelewski, D. Emin, and C. B. Mullins, "Unravelling small-polaron transport in metal oxide photoelectrodes," J. Phys. Chem. Lett. **7**, 471–479 (2016).
[158]S. Wang, P. Chen, Y. Bai, J.-H. Yun, G. Liu, and L. Wang, "New $BiVO_4$ dual photoanodes with enriched oxygen vacancies for efficient solar-driven water splitting," Adv. Mater. **30**, 1800486 (2018).
[159]W. Zhang, L. Song, J. Cen, and M. Liu, "Mechanistic insights into defect-assisted carrier transport in bismuth vanadate photoanodes," J. Phys. Chem. C **123**, 20730–20736 (2019).
[160]W. J. Yin, S. H. Wei, M. M. Al-Jassim, J. Turner, and Y. Yan, "Doping properties of monoclinic $BiVO_4$ studied by first-principles density-functional theory," Phys. Rev. B **83**, 1–11 (2011).
[161]Y. Yuan, Y. Huang, F. Ma, Z. Zhang, and X. Wei, "Effects of oxygen vacancy on the mechanical, electronic and optical properties of monoclinic $BiVO_4$," J. Mater. Sci. **52**, 8546–8555 (2017).
[162]Y. K. Kho, W. Y. Teoh, A. Iwase, L. Mädler, A. Kudo, and R. Amal, "Flame preparation of visible-light-responsive $BiVO_4$ oxygen evolution photocatalysts with subsequent activation via aqueous route," ACS Appl. Mater. Interfaces **3**, 1997–2004 (2011).
[163]C. Freysoldt, B. Grabowski, T. Hickel, J. Neugebauer, G. Kresse, A. Janotti, and C. G. Van de Walle, "First-principles calculations for point defects in solids," Rev. Mod. Phys. **86**, 253 (2014).
[164]S. Selim, E. Pastor, M. García-Tecedor, M. R. Morris, L. Francas, M. Sachs, B. Moss, S. Corby, C. A. Mesa, S. Gimenez *et al.*, "Impact of oxygen vacancy occupancy on charge carrier dynamics in $BiVO_4$ photoanodes," J. Am. Chem. Soc. **141**, 18791–18798 (2019).
[165]T. W. Kim, Y. Ping, G. A. Galli, and K.-S. Choi, "Simultaneous enhancements in photon absorption and charge transport of bismuth vanadate photoanodes for solar water splitting," Nat. Commun. **6**, 9769 (2015).
[166]J. K. Cooper, S. B. Scott, Y. Ling, J. Yang, S. Hao, Y. Li, F. M. Toma, M. Stutzmann, K. V. Lakshmi, and I. D. Sharp, "Role of hydrogen in defining the *n*-type character of $BiVO_4$ photoanodes," Chem. Mater. **28**, 5761–5771 (2016).
[167]J. Hu, W. Chen, X. Zhao, H. Su, and Z. Chen, "Anisotropic electronic characteristics, adsorption, and stability of low-index $BiVO_4$ surfaces for photoelectrochemical applications," ACS Appl. Mater. Interfaces **10**, 5475–5484 (2018).
[168]F. S. Hegner, Dataset for: Versatile nature of oxygen vacancies in bismuth vanadate bulk and (001) surface, 2019, https://doi.org/10.19061/iochem-bd-1-133.
[169]N. N. Greenwood and A. Earnshaw, *Chemistry of the Elements* (Elsevier Science, Amsterdam, The Netherlands, 2012).
[170]M. V. Ganduglia-Pirovano and J. Sauer, "Stability of reduced V_2O_5 (001) surfaces," Phys. Rev. B **70**, 045422 (2004).
[171]M. D. Rossell, P. Agrawal, A. Borgschulte, C. Heert, D. Passerone, and R. Erni, "Direct evidence of surface reduction in monoclinic $BiVO_4$," Chem. Mater. **27**, 3593–3600 (2014).
[172]Y. Hermans, S. Murcia-López, A. Klein, and W. Jaegermann, "$BiVO_4$ surface reduction upon water exposure," ACS Energy Lett. **4**, 2522–2528 (2019).
[173]M. Gerosa, F. Gygi, M. Govoni, and G. Galli, "The role of defects and excess surface charges at finite temperature for optimizing oxide photoabsorbers," Nat. Mater. **17**, 1122–1127 (2018).
[174]M. D. Wilkinson, M. Dumontier, I. J. Aalbersberg, G. Appleton, M. Axton, A. Baak, N. Blomberg, J.-W. Boiten, L. B. da Silva Santos, P. E. Bourne, J. Bouwman, A. J. Brookes, T. Clark, M. Crosas, I. Dillo, O. Dumon, S. Edmunds,

C. T. Evelo, R. Finkers, A. Gonzalez-Beltran, A. J. G. Gray, P. Groth, C. Goble, J. S. Grethe, J. Heringa, P. A. C. 't Hoen, R. Hooft, T. Kuhn, R. Kok, J. Kok, S. J. Lusher, M. E. Martone, A. Mons, A. L. Packer, B. Persson, P. Rocca-Serra, M. Roos, R. van Schaik, S.-A. Sansone, E. Schultes, T. Sengstag, T. Slater, G. Strawn, M. A. Swertz, M. Thompson, J. van der Lei, E. van Mulligen, J. Velterop, A. Waagmeester, P. Wittenburg, K. Wolstencroft, J. Zhao, and B. Mons, "The FAIR guiding principles for scientific data management and stewardship," Sci. Data **3**, 160018 (2016).

[175]National Science and Technology Council (U.S.), Materials genome initiative for global competitiveness, 2011.

[176]M. Álvarez Moreno, C. De Graaf, N. López, F. Maseras, J. M. Poblet, and C. Bo, "Managing the computational chemistry big data problem: The ioChem-BD platform," J. Chem. Inf. Model. **55**, 95–103 (2014).

[177]M. Capdevila-Cortada, Dataset for: Mechanism and microkinetics of methanol synthesis via CO_2 hydrogenation on indium oxide, 2018, https://doi.org/10.19061/iochem-bd-1-63.

[178]M. Rellán-Piñeiro, Dataset for: One oxygen vacancy, two charge states: Characterization of reduced α-MoO_3 (010) through theoretical methods, 2018, https://doi.org/10.19061/iochem-bd-1-59.

[179]R. García Muelas, Dataset for: Atomic-scale engineering of indium oxide promotion by palladium for methanol production via CO_2 hydrogenation, 2019, https://doi.org/10.19061/iochem-bd-1-106.

[180]N. Daelman, Dataset for: Dynamic charge and oxidation state of Pt/CeO_2 single-atom catalysts, 2019, https://doi.org/10.19061/iochem-bd-1-78.

[181]N. Dragoe and D. Bérardan, "Order emerging from disorder," Science **366**, 573–574 (2019).